Mass Transfer During Freezing in Rat Prostate Tumor Tissue

Ramachandra V. Devireddy, David J. Smith, and John C. Bischof
Bioheat and Mass Transfer Laboratory, Dept. of Mechanical Engineering, University of Minnesota, Minneapolis, MN 55455

Cryosurgery for treating prostate cancer is hampered by an incomplete understanding of the mechanisms whereby tissue destruction is achieved during freezing. The two known biophysical mechanisms of injury, intracellular ice formation and cellular dehydration injury (solute effects), have not been quantified within tumor tissue. Freeze substitution microscopy and a differential scanning calorimeter (DSC) were used to quantify freeze-induced dehydration within Dunning AT-1 rat prostate tumor tissue. Stereological analysis of histological tumor sections was used to obtain the initial cellular (V_o), interstitial, and vascular volumes of the AT-1 tumor tissue. A Boyle-van't Hoff (BVH) plot was then constructed by examining freeze substituted micrographs of equilibrium cooled tissue slices to obtain the osmotically inactive cell volume, $V_b = 0.25V_o$. Obtaining dynamic cellular water transport information from the freeze substitution microscopy data proved difficult because of the artifact added by the high interstitial volume ($\sim 35\%$). Since the DSC technique does not suffer from this artifact, a model of water transport was fit to the DSC water transport data at 5°, 10° and 20°C/min to obtain the combined best fit membrane permeability parameters of the embedded AT-1 tumor cells, assuming either a Krogh cylinder geometry or a spherical cell geometry. Numerical simulations were also performed to generate conservative estimates of intracellular ice volume (IIV) in the tumor tissue at various cooling rates typical of those experienced during cryosurgery (≤ 100°C/min). Water transport data in tumor systems with significant interstitial spaces can be obtained by using histology and the low-temperature microscopy methods to obtain the initial and final tissue cell volumes, respectively, and the DSC technique to obtain the dynamic volume changes during freezing.

Introduction

The use of freezing to destroy living tumorous tissues termed *cryosurgery* has shown reasonable success in the treatment of human prostate carcinoma (Onik et al., 1995). [*In 1996, over 317,000 new cases of human prostate carcinoma were diagnosed in the U.S. alone and over 41,000 patients died from this disease (American Cancer Society, 1996).*] Freezing is usually achieved by conduction when a metallic probe, through which a cryogen (usually liquid nitrogen) is circulated, is brought into contact with the tumor to be treated. Cryogen flowing through the probe tip causes the metal-tipped probe temperature to drop, extracting heat from the tumor and causing it to freeze. As the freezing interface begins to move out away from the probe, the cooling rate experienced by the tumor changes from very fast ($\sim 50-100$°C/min) near the probe tip to very slow cooling rates (< 5°C/min) at the edge of the cryosurgical iceball. In order to be effective, the cryosurgical procedure must cause lethal freeze-induced damage throughout the tumor. Thus, it is important to know precisely the biophysical response to the tumor tissue in different regions of the iceball, as these biophysical changes are known to affect tissue viability. The focus of this study is to quantify the biophysical response in Dunning AT-1 rat prostate tumor tissue during freezing at controlled cooling rates representative of those experienced in an iceball during

Correspondence concerning this article should be addressed to J. C. Bischof.

cryosurgery. The AT-1 rat prostate tumor cell line was chosen as the experimental tumor model, since it has been shown to have microscopic and macroscopic similarity to human prostate carcinoma and can be destroyed by cryosurgery.

The two important biophysical responses experienced by the tumor cells in the presence of vascular/extracellular ice during freezing are water transport (or mass transfer) out of the tissue cells (that is, cellular dehydration) and intracellular ice formation (IIF). These biophysical responses are directly coupled to tissue injury as described by Mazur's two factor hypothesis: (a) at low cooling rates, freezing injury occurs due to high solute concentration effects caused by cellular dehydration (Lovelock, 1953) and decreasing unfrozen fraction of the vascular/extracellular space (Mazur, 1970); (b) at high cooling rates, freezing injury occurs due to IIF (Mazur, 1970). [*The exact magnitude of the low and high cooling rates are specific to a cell type and need to be experimentally determined.*] Although these biophysical events have been extensively studied in single cells with cryomicroscopy techniques (see reviews by Diller, 1982; McGrath, 1988), similar experimental data in whole tissues are only now emerging (Pazhayannur and Bischof, 1997; Devireddy and Bischof, 1998). The early qualitative and uncontrolled slow freezing studies by Trump et al. (1964) and Love (1966) were useful in showing that ice forms preferentially in the vascular/extracellular space, thereby inducing cellular dehydration into this space. Rubinsky et al. (1987) and Bischof et al. (1993) studied the biophysical response of liver tissues to controlled rate freezing using a directional solidification stage and low-temperature microscopy techniques. Although an improvement over the earlier uncontrolled freezing studies (Trump et al., 1964; Love, 1966), the controlled rate studies (Rubinsky et al., 1987; Bischof et al., 1993) cannot extract information on the dynamic water transport in the tissue cells, since only the end-state after freezing was imaged. This work presents dynamic and quantitative water transport data for Dunning AT-1 rat prostate tumor tissue during freezing using the two techniques developed in our lab, a low-temperature microscopy technique (Pazhayannur and Bischof, 1997) and a method using differential scanning calorimetry (Devireddy et al., 1998; Devireddy and Bischof, 1998).

Theoretical Background

During freezing of tissue systems, ice tends to form first in the vascular/extracellular space of whole tissues (Rubinsky et al., 1987; Bischof et al., 1993). The presence of vascular/extracellular ice creates a small, highly concentrated unfrozen saline fraction which induces a chemical potential difference across the tissue cell membrane. Water transport across the membrane of a spherical cell during freezing in the presence of extracellular ice has been modeled by Mazur (1963), whose model was later modified by Levin et al. (1976). This model of water transport assumes an idealized biological cell as an open thermodynamic system having a semi-permeable membrane boundary (that is, permeable to water and impermeable to solutes). The model also assumes: (a) no pressure gradients exist across the cell membrane (a good assumption for mammalian cells and isolated plant protoplasts); (b) temperature differentials across the cell membrane are negligible (~ 0.01 K for most practical purposes, as shown by Hua et al., 1982); (c) no concentration gradients exist except across the cell membrane (McGrath, 1988). In its simplest form the water transport model can be represented as

$$\frac{dV}{dT} = -\frac{L_p A_c RT}{B\upsilon_w}\left(\ln \frac{a_i^w}{a_o^w}\right) \tag{1}$$

where V is the cell volume, T is the absolute temperature (K), L_p is the tissue cell membrane permeability to water, A_c is the area ($2\pi r_{\upsilon o}$L) of membrane surface available for water transport, R is the universal gas constant, B is the cooling rate (K/min), υ_w is the partial molar volume of water, and a^w is the chemical activity of water, where the subscripts i and o stand for the intracellular fluid and extracellular fluid, respectively.

Quantitative use of the above thermodynamic model requires a more complete specification of the chemical activities of the extracellular and the intracellular solutions, along with the membrane water permeability. The extracellular solution is assumed to be composed of a binary solution consisting of water and sodium chloride and can be modeled using the equilibrium properties of a solid/liquid solution. The Gibbs-Helmholtz equation relates the equilibrium water activity in the solution as a function of temperature as

$$\frac{\partial(\ln a_w)}{\partial T} = \frac{\Delta H_f}{RT^2} \tag{2}$$

where ΔH_f is the latent heat of fusion of water (assumed to be a constant at 335 mJ/mg). Integrating the above expression yields the extracellular water activity as

$$\ln a_w = \frac{\Delta H_f}{R}\left[\frac{1}{T_R} - \frac{1}{T}\right] \tag{3}$$

where T_R is the reference temperature (273.15 K).

The intracellular solution is typically modeled as an ideal and dilute solution so that the chemical activity of the internal water is equal to the mole fraction of water (Mazur, 1963)

$$a_w^i = X_w^i \tag{4}$$

Although the intracellular solution is neither ideal nor dilute, Levin et al. (1977) have shown that the inclusion of nonidealities has a negligible effect on subzero cell volume modeling. Neglecting the cell membrane volume and recognizing that some of the intracellular fluid may be bound water, that is, water which is not free to move across the cell membrane in response to an osmotic gradient (which is included in the osmotically inactive cell volume term V_b), the mole fraction of intracellular water is given as

$$X_w^i = \frac{V - V_b}{(V - V_b) + \varphi_s n_s \upsilon_w} \tag{5}$$

In addition, φ_s is the disassociation constant for sodium chloride (2), n_s is the number ($C_i(V_o - V_b)$) of moles of salt ions. Substituting Eqs. 3 and 5 in Eq. 1, one arrives at the Mazur

model of water transport (Mazur, 1963),

$$\frac{dV}{dT} = -\frac{L_p A_c RT}{Bv_w} \times \left[\ln\frac{(V-V_b)}{(V-V_b)+\varphi_s n_s v_w} - \frac{\Delta H_f}{R}\left(\frac{1}{T_R}-\frac{1}{T}\right)\right] \quad (6)$$

The temperature dependence of the membrane permeability ($m^3/N \cdot s$ ($\mu m/min \cdot atm$)) to water (L_p) is expressed as an Arrhenius relationship (Levin et al., 1976)

$$L_p = L_{pg}\exp\left[-\frac{E_{L_p}}{R}\left(\frac{1}{T}-\frac{1}{T_R}\right)\right] \quad (7)$$

where L_{pg} is the permeability of the cell membrane to water at a reference temperature (273.15 K) and E_{Lp} is the apparent activation energy (J/mole(kcal/mole)) of the permeation (water transport) process. And, finally, to complete this water transport model, a geometry needs to be selected which defines the cell volume V and the surface available for water transport A_c.

The water transport model described above was originally developed by Mazur (1963) for spherical cells and was later extended to model tissue cell volume changes during freezing using a simple two-component Krogh cylinder approach (Rubinsky and Pegg, 1988; Pazhayannur and Bischof, 1997). Figure 1 shows the Krogh cylinder model used in this study and the corresponding dimensions including the radius of the extracellular space ($r_{vo} = r_{vas} + r_{int}$ where r_{vas} and r_{int} are the radius (μm) of the microvascular channels and the interstitial spaces in the extracellular matrix, respectively), the distance (μm) between the microvascular channels (ΔX), and the axial length of the Krogh cylinder (L). In the Krogh cylinder model the cellular space with volume V is modeled as the box surrounding the cylinder ($V = L\Delta X^2 - \pi r_{vo}^2 L$), that is, the extracellular volume including the interstitial and vascular spaces is modeled as the cylinder of volume $\pi r_{vo}^2 L$ and the effective membrane surface area available for water transport (mass transfer) during the freezing process is assumed to be a constant, $A_c = 2\pi r_{vo} L$. Note that the length (μm) of the Krogh cylinder L is not important in the Krogh model (that is, under conditions of uniform temperature throughout the Krogh unit, the water transport simulations obtained using Eqs. 6 and 7 are identical with different Ls). This is because the ratio of cellular volume V and the available membrane surface area A_c is independent of the length of the Krogh unit L. The use of the Krogh model necessitates several other assumptions to be made (as described by Rubinsky and Pegg, 1988 and Pazhayannur and Bischof, 1997) which include: (a) the tissue is composed of a number of identical Krogh units all experiencing the same thermal history; (b) axial flow of blood in the vasculature is neglected; (c) a single lumped permeability for water transport between the intracellular and vascular/extracellular spaces is assumed. In this study two other assumptions were made to account for the presence of a significant amount of interstitial spaces in tumor tissue cells (Jain, 1987): (a) the resistance of interstitial spaces to water transport (mass transfer) is negligible when compared to the cell membrane resistance. Thus, the tumor cell membrane is assumed to be the primary resistance to mass transfer (water transport) during freezing (see Appendix); (b) interstitial space was included as a part of the extracellular space instead of a separate compartment thus maintaining the two compartment nature of the Krogh model (see Figure 1). A theoretically determined temperature-volume history of a cell during freezing can be predicted by integrating Eqs. 6 and 7, assuming that the cell volume (V) is equal to the isotonic cell volume (V_o) at temperature T_{ph}, the phase change temperature of the extracellular media. The unknown membrane permeability parameters of the model, reference membrane permeability L_{pg} and the apparent activation energy of the membrane permeability E_{Lp}, are then determined by curve-fitting the water transport model to experimentally obtained water transport (mass transfer) data during freezing.

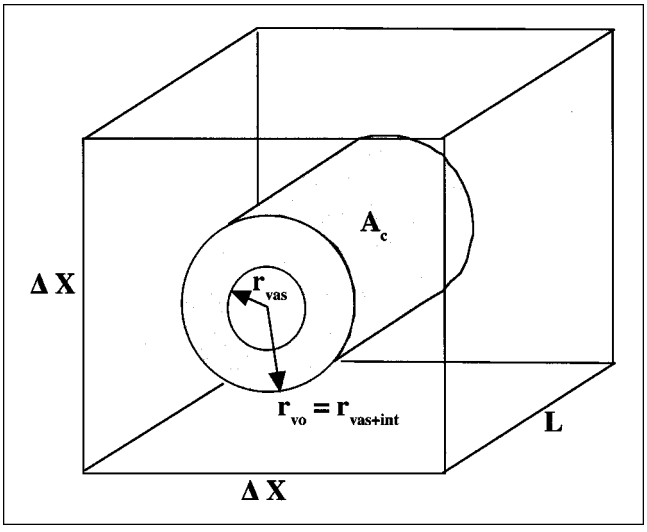

Figure 1. Krogh cylinder, a representation of a Dunning AT-1 tumor tissue unit.

The Krogh cylinder dimensions for AT-1 Dunning Rat Prostate Tumor tissue are: ΔX the distance between the microvascular channels = 17.9 μm, r_{vo} the initial radius of the extracellular space = 6.5 μm, and L the axial length of the Krogh cylinder = 18.1 μm.

Materials and Methods

AT-1 tumor tissue growth

Tumors were seeded by subcutaneous injection of 2×10^6 AT-1 cells in 100 μL of Hank's balanced salt solution in the flank region of $\sim$250 gram male Copenhagen rats (Harlan-Sprague-Dawley, Inc., Indianapolis, IN). Tumors were grown to a size of 2–3 cm in the largest dimension. Upon excision, the tumors were placed in a petri dish with serum-free RPMI culture media (Celox, Inc., Hopkins, MN) on ice and divided along the long axis of the tumor using a razor blade. Tumor tissue from the periphery of each tumor half was used in the freezing experiments in order to avoid the possibility of taking necrotic tissue which is sometimes found in the core of these tumors. Tumor tissue was cut by either mincing with a razor blade or using a Stadie Riggs microtome to a thickness of 500 μm (Thomas Scientific, Inc.). The tissue slices were

then prepared for low-temperature microscopy or DSC experiments as described below. Anoxic (lack of oxygen) time of the tumor samples in RPMI on ice never exceeded 2.5 h.

Low temperature microscopy experiments

The freezing experiments were performed on a directional solidification stage based on the design of Rubinsky and Ikeda (1985), and described in Pazhayannur and Bischof (1997). Briefly, two copper platforms fitted with type *T* thermocouples (Omega Tech. Corp., Stamford, CT) are cooled by an internal liquid nitrogen flow and heated by a foil heater; platform temperatures are regulated by control of heater voltages by Fuji digital controllers (Total Temperature Instrumentation, Williston, VT). The spacing between the platforms is set by the user. The sample to be frozen is placed on a glass microslide, and propagated across the gap between the platforms. The propagation speed, platform spacing and platform temperatures are set to achieve the desired cooling rate and end temperature for the freezing experiment.

In order to investigate a very fast rate of freezing ($\geq$ 1,000°C/min), a copper block slam freezing procedure was used. The tumor tissue samples ($n = 5$ each ≤ 1 mm^3) were placed on a standard glass microscope microslide and then brought into intimate contact with a highly polished copper block (2 in.$\times$2 in.$\times$0.5 in.) which, until use, was in thermal equilibrium with liquid nitrogen at -196°C. The microslide with the frozen tumor tissue samples was then quickly immersed in a petri dish with liquid nitrogen. While immersed, the samples were carefully detached from the microslide with prechilled forceps. The samples were stored in 1.5 ml cryovials in liquid nitrogen for further microscopic preparation and analysis.

Tissue-freeze substitution

In order to visualize the tumor tissue morphology in the frozen state, fixation must take place at a low temperature; the technique of freeze substitution, which is generally described by Echlin (1992), has previously been used on rat (Pazhayannur and Bischof, 1997) and human (Bischof et al., 1993) liver tissue, and will also be used in this study with minor modifications. To begin freeze substitution, 1 mL of a 3% (by weight) osmium tetroxide (Sigma Chemical Co., St. Louis, MO) in acetone solution at -90°C was added to each cryo-vial containing up to 5 tissue samples, and the vial was then placed in a freeze substitution (FS) device (Bal-Tec, Middlebury, CT) at -90°C for 24 h, at -60°C for 2 h, -30°C for 2 h, and 0°C for 30 min. During this time, the osmium fixed and stained the membranous cell structures dark, while the acetone replaced all the water (ice) in the sample.

After fixation by freeze substitution, samples were gradually brought back to room temperature and dehydrated by repeated washing in 100% acetone. Samples were then infiltrated with Quetol resin (Ted Pella Inc., Redding, CA) at room temperature for >12 h, during which time the resin replaced the acetone in the sample. The samples were then transferred to Beem capsules (Polysciences, Inc., Warrington, PA) and embedded in additional resin. The embedded samples were held in a dry oven at 70°C for >12 h to polymerize the resin. The samples were then sectioned on a Reichert Ultracut microtome (Leica, Vienna, Austria) to a thickness of 0.5 μm. The tissue sections were mounted on glass microslides and stained with Toluidine Blue (Sigma Chemical Co., St. Louis, MO) in preparation for image analysis.

Photomicrographs of the tissue sections were obtained by imaging through a Newvicon camera (Hamamatsu-Photonics, Bridgewater, NJ) attached to a Nikon Labophot light microscope (Nikon Inc., Melville, NY) and digitized on a workstation computer with a frame grabber (SGI, Mountainview, CA). The image analysis procedure used to obtain volumetric data from the photomicrographs is described in detail by Pazhayannur and Bischof (1997). Adobe Photoshop software (Adobe Systems Inc., Mountain View, CA) was used to separate which areas of the micrograph were cellular (darkly stained) and which were extracellular (lightly stained); then, NIH-Image software (NIH, Bethesda, MD) was used to measure the ratio of cellular to extracellular area. The volumes of the cellular and extracellular spaces were assumed to be directly proportional to the areas measured (stereologically). These measured volumes were then imposed on the Krogh model (Figure 1) by assigning appropriate dimensions, as described below.

Krogh model dimensions

The histology of control tumor tissue was assessed by fixing the tissue sample in a Bouin's solution followed by paraffin embedding, sectioning, and hematoxylin and eosin staining (as described in Bischof et al., 1997). Stereological measurements were performed on these micrographs to obtain the Krogh model dimensions: the distance between the microvascular channels (ΔX) was measured as the shortest distance between the centers of two adjacent parallel microvascular channels, the radius of the extracellular spaces (r_{vo}) was determined such that the percentage of total volume (or area) occupied by the cylinder in the Krogh model ($\pi r_{vo}^2/\Delta X^2$) corresponds to the percentage of the measured extracellular spaces (including vascular and interstitial spaces) in the control micrograph, and, finally, the axial length of the cylinder L was chosen such that the cellular volume V in the Krogh cylinder model corresponds to the volume of a single isolated AT-1 cell $\sim$3,400 μm^3 based on a spherical cell diameter of 18.7 μm (Smith et al., 1997).

Equilibrium and dynamic cooling

The osmotically inactive cell volume (obtained by constructing a Boyle van't Hoff plot from equilibrium cooled micrographs) and the dynamic volumetric response for AT-1 tumor tissue cooled at 5°C/min were determined in this work. In order to obtain the AT-1 tumor tissue morphology during equilibrium cooling conditions, the samples were frozen at 2°C/min on the directional solidification stage to various end temperatures (-4°, -6°, -8°, -10°, and -20°C) and held for 15 min before being slam frozen ($>$1,000°C/min). Snapshots of the AT-1 tumor tissue morphology at several temperatures during a dynamic freezing process were obtained by freezing the tumor tissue samples on the directional solidification stage at 5°C/min to various end temperatures (-4°, -6°, -8°, -10°, and -20°C) followed by slam freezing as described in detail by Pazhayannur and Bischof (1997). Micrographs of AT-1 tumor tissue cooled at various cooling rates ($>$1,000°C/min, 400°, 100°, 50°, 10°, and 5°C/min) to a low

end temperature of -20°C were also obtained to determine the cooling rate above which the dominant biophysical response is intracellular ice formation (IIF). The intracellular volumes measured at each temperature were normalized by the intracellular volume of the slam frozen control tissue sample.

Effect of interstitium on image analysis

We were unable to devise a quantitative and reliable way to distinguish between the interstitial spaces and cellular spaces at subzero temperatures in the freeze substituted tissue micrographs. However, we contend that the high water content in tumor interstitium should cause the interstitial volume to collapse substantially at low subzero temperatures (< -10°C) during freeze-induced dehydration. Interstitial spaces are predominantly collagen with glycosaminoglycans (GAGs) and other molecules that are designed to trap large amounts of water (Nugent and Jain, 1984). It is estimated that 1 mg of tumor collagen or interstitial spaces contains 0.6 mL of water (Bert and Pearce, 1984) or ~ 0.0017 g of tumor collagen/g of water (that is, 99.83% of tumor interstitial collagen matrix is water). To support our contention, a literature search was performed to obtain light micrographs of frozen solutions that approximate the water bearing abilities of the tumor interstitial spaces (that is, gelatin and/or starch solutions). We found by stereological analysis of 7% starch solution ($\gg 0.017$% collagen) micrographs obtained by Meryman (1966) that only 10% of the total volume was stained, when cooled at 1–2°C/min (or equilibrium cooling) to -10°C. The rest of the space (~ 90%) was occupied by pure ice crystals. Now applying this result to the interstitium in our sample tissue shown in Figure 2, we contend that the original interstitium volume (35% of total) will be reduced to ~ 3.5% of total volume at -10°C and below, provided complete dehydration has occurred. Thus, a worst case error due to the presence of the interstitium in the measurement/estimation of osmotically inactive cell volume V_b using the Boyle-van't Hoff plot is $\sim 0.035 V_o$. This small error in the value of V_b was neglected in this study, particularly because this error will be reduced to $\sim 0.0009 V_o$, if one takes into account that 7% starch solution has a concentration that is ~ 41.2 times that of the tumor interstitial collagen matrix (7% vs. 0.17%). Nevertheless in the expanded (hydrated) state (at $T \geq -8$°C), the interstitial spaces may contribute a significant error in the estimation of the cellular volumes for both the equilibrium (2°C/min) and dynamic (≥ 5°C/min) water transport data. To address this problem, we used a DSC technique to measure dynamic water transport data, as described next. The DSC technique does not suffer from this extracellular artifact, as it is independent of the geometry of the sample.

DSC experiments

Sample Preparation. Experiments were performed on excised tumor tissue slices. The tumor tissue was cut into small pieces (1–1.5 mm^3) using a razor blade. The tumor tissue slices were then patted externally using a blotting paper and their weight was measured (1–1.5 mg). The samples were then placed in standard aluminum sample pans (Perkin Elmer Corporation, Norwalk, CT) and a small drop (< 8 μL) of isotonic PBS (Celox, Inc., Hopkins, MN) was added to keep the tissue slice in an isotonic environment. A natural ice nucleator *Pseudomonas syringae* (ATCC, Rockville, MD) was added (0.5 to 1 mg) before the pans were sealed and the DSC pans were reweighed to measure the total sample weight before the DSC experiments were performed. The ice nucleating agent *P. syringae* always nucleated the vascular/extracellular space at temperatures ≥ -4°C in order to avoid damaging intracellular ice formation, which occurs predominantly at temperatures below -5°C in most cell systems (Toner, 1993). The total sample weight has always kept ≤ 10 mg.

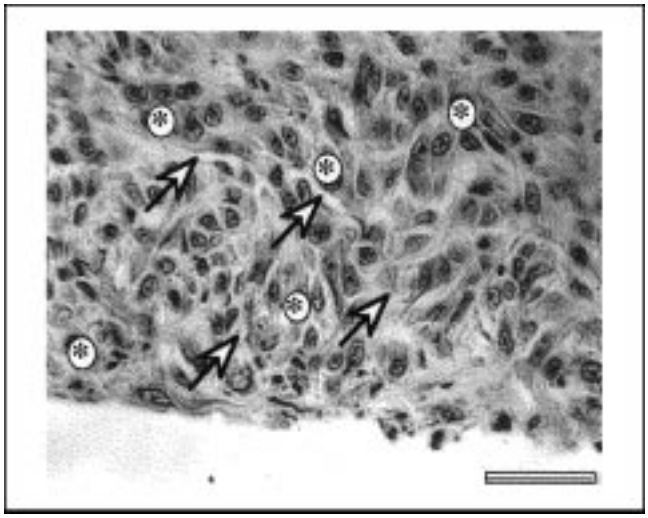

Figure 2. Histology of AT-1 tumor tissue line.

The sample was fixed in Bouin's solution, embedded in paraffin and stained with hematoxylin and eosin. Dark stained, optically dense areas (represented by stars), correspond to tumor cells, while the optically transparent areas (represented by arrows), correspond to the vasculature and extracellular matrix (interstitial spaces) of the tumor. (Scale bar = 40 μm.)

DSC Dynamic Cooling Protocol. The DSC protocol developed to measure water transport out of tumor cells is the same as the one detailed in Devireddy et al. (1998) for single cell suspension systems and by Devireddy and Bischof (1998) for a mammalian (normal male Sprague Dawley rat) liver tissue system. DSC experiments were conducted at cooling rates of 5°, 10°, and 20°C/min. To ensure the accuracy and repeatability of the experimental data, the limitations of the DSC machine were studied and a set of calibration and control experiments were performed as described previously by Devireddy et al. (1998).

Step 1: The sample (tumor slices + isotonic PBS) + 0.5 to 1 mg of *P. syringae* bacteria initially at 4°C was cooled at 5°C/min until the vascular/extracellular ice nucleated (usually around -3.5°C).

Step 2: At the time of nucleation, the sample was manually triggered to thaw at a warming rate (10°C/min) such that the phase change temperature of the isotonic media T_{ph} (~ -0.53°C) was reached (but not overshot) and ice remained in the extracellular solution. The phase change temperature can be obtained by using the osmolality relationship ($\text{Osm}^{-1} = 1.858/\Delta T$; $\Delta T = 273.15 - T$, K) and the osmolality

of the isotonic media (which is the osmolality of most biological fluids, ~ 0.285 Osm); thus, $\Delta T = 0.285 * 1.858 = \sim 0.53$ K or $T_{ph} = -0.53$°C.

Step 3: The sample was then cooled to −50°C at the specified cooling rate (5°, 10° or 20°C/min) causing the tissue cells to undergo cellular dehydration, and the initial heat release due to the media mixed with osmotically active cells was measured ($q_{ec+cw} = \sim 2{,}330$ mJ or ~ 233 mJ/mg) (see Figure 3).

Step 4: The sample was reequilibrated at −0.53°C by thawing at 100°C/min.

Step 5: To help differentiate between the heat released by the media and the intracellular fluid in Step 3, the tumor cell membranes were compromised by cooling the sample at a high cooling rate (200°C/min) down to −50°C.

Step 6: Step 4 was repeated. Since all the cells have compromised membranes, the intracellular water, proteins and salts now are continuous with the extracellular solution (the membrane barrier is lost) as previously suggested by Körber et al. (1991).

Step 7: The sample was then cooled to −50°C at the specified cooling rate (5°, 10°, or 20°C/min) to measure the final heat release due to lysed or osmotically inactive cells mixed with media ($q_{ec+cw+cd} = \sim 2{,}212$ mJ or ~ 212 mJ/mg) (see Figure 3).

To confirm that the fast cooling run in Step 5 (200°C/min to −50°C) compromised the membrane integrity of all the AT-1 tumor tissue cells in the sample, Steps 6 and 7 were repeated and no further decrease in the measured heat release ($q_{ec+cw+cd}$) was found. A separate control experiment was also performed using tumor tissue which was destroyed by leaving it in a cold ischemic environment for a week. The tissue slices which underwent this ischemia were assumed to be lysed or osmotically inactive. DSC experiments were performed using these lysed tissue slices as described above and Δq_{dsc} ($= q_{ec+cw} - q_{ec+cw+cd}$) was measured to be zero and the measured heat release was further found to be equal to $q_{ec+cw+cd}$ obtained in Step 7 of the DSC cooling protocol (± 4 mJ). This small variation in the final heat release $q_{ec+cw+cd}$ (~ 4 mJ or ~ 0.4 mJ/mg) was neglected as it represents $< 3.4\%$ of the measurement of interest in a typical DSC experiment Δq_{dsc} (~ 118 mJ or ~ 11.8 mJ/mg). These results confirm that the fast cooling run in Step 5 (200°C/min to −50°C) compromised the membrane integrity of all the AT-1 tumor tissue cells in the sample.

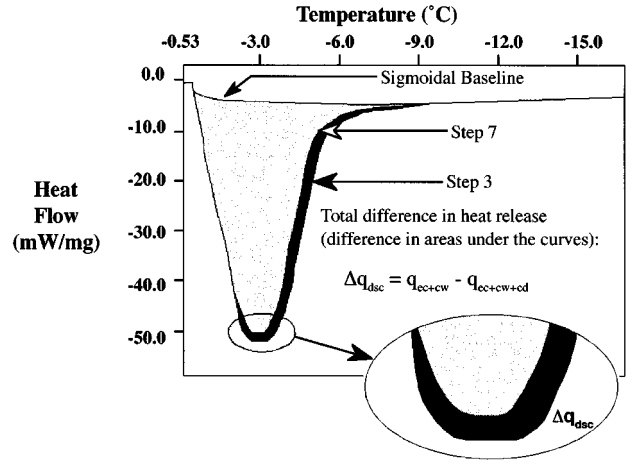

Figure 3. Superimposed heat flow thermograms obtained during the first (Step 3) and last (Step 7) of the DSC cooling protocol for AT-1 tumor tissue system for a cooling rate (B) of 5°C/min.

The lower curve and upper curves correspond to the heat flow thermogram measured in Step 3 and Step 7 of the DSC cooling protocol, respectively. Note that the heat flow measured (heat released) in Step 7 is always less than the heat flow measured (heat released) in Step 3. The total difference between q_{ec+cw} (Step 3) and $q_{ec+cw+cd}$ (Step 7) is denoted as Δq_{dsc}. The heat flow (mW/mg) is plotted along the *y*-axis and the subzero temperatures (°C) are plotted along the top *x*-axis. The negative axis for the heat flow on the *x*-axis implies an exothermic heat release in the DSC sample.

Translation of Heat Release to Tumor Tissue Volume Data. The heat release measurements of interest are Δq_{dsc} and $\Delta q(T)_{dsc}$ which are represented by the total and fractional difference between the heat releases measured by integration of the heat flows in Steps 3 and 7, respectively, using the DSC-7 (Perkin-Elmer software). The total difference in the integrated heat release between the base line (constant and sigmoidal) and the actual thermogram in the two cooling runs (Step 3 and Step 7) is denoted as Δq_{dsc} ($= q_{ec+cw} - q_{ec+cw+cd}$) and is shown in Figure 3. The fractional difference in the integrated heat release from T_{ph} down to a subzero temperature T is denoted by $\Delta q(T)_{dsc}$ ($= q(T)_{ec+cw} - q(T)_{ec+cw+cd}$). This difference in heat release has been shown to be related to cell volume changes in cell suspensions (Devireddy et al., 1998) and in normal rat liver tissue systems (Devireddy and Bischof, 1998) as

$$\frac{V_o - V(T)}{V_o - V_b} = \frac{\Delta q(T)_{dsc}}{\Delta q_{dsc}} \tag{8}$$

We can rearrange and write a simplified equation to measure water transport data from the DSC measured heat releases $\Delta q(T)_{dsc}$ and Δq_{dsc} as

$$V(T) = V_0 - \frac{\Delta q(T)_{dsc}}{\Delta q_{dsc}} \cdot (V_o - V_b) \tag{9}$$

The DSC water transport data obtained using Eq. 9, was shown to generate statistically similar data ($> 95\%$ confidence level using the Student's t-test) to that obtained using a standard cellular cryomicroscopy technique in a cell suspension system (Devireddy et al., 1998) and also to the water transport data obtained using the low-temperature microscopy method in a normal rat liver tissue system (Devireddy and Bischof, 1998). Since the use of Eq. 9 to generate water transport data from DSC measured heat release readings has been validated in the above mentioned cell and tissue systems, it is reasonable to assume that it can be used to generate the water transport data in a tumor tissue system as well. The only other unknowns needed in Eq. 9 apart from the DSC heat release readings are the Krogh cylinder dimensions (L, ΔX, r_{vo}), the isotonic cell volume V_o, and the osmotically inactive cell volume V_b, which were all obtained us-

ing histology and low-temperature microscopy techniques as described earlier.

Numerical methods

A nonlinear least-squares curve fitting technique was implemented in a computer program to calculate the membrane permeability parameters (L_{pg} and E_{Lp}) that best fit the volumetric shrinkage data obtained from the DSC and the low-temperature microscopy experiments as previously described (Bevington and Robinson, 1992). The computer program used a fourth-order Runge Kutta method to calculate the volume as a function of temperature (based on selected parameters and cooling conditions) and then compared the simulated water transport volumes to experimental data. The optimal fit of Eq. 6 to the experimental data was obtained by selecting a set of parameters which minimized the residual variance χ^2 and maximized a goodness of fit parameter R^2 (Montgomery and Runger, 1994).

In order to predict the membrane permeability parameters that produced a combined best fit to the experimental water transport data at two or more cooling rates, the nonlinear curve fitting code was slightly modified. A new residual variance χ^2 was calculated as a sum of the residual variances at all the cooling rates, where the model predictions $y(x_i)$ were obtained using one set of membrane permeability parameters for all the cooling rates. The goodness of fit parameter R^2 was calculated using the new residual and total variances. A set of combined best fit membrane permeability parameters that maximized R^2 for all the cooling rates was found. All the curve fitting results presented have an R^2 value greater than or equal to 0.98 indicating that there was a good agreement between the experimental data points and the fit calculated using the estimated membrane permeability parameters.

Computer Simulations. To simulate biophysical response of tissue under a variety of cooling rates, the best fit parameters were substituted in Eq. 7 and the water transport equation (Eqs. 6 and 7) was numerically solved using a 4th-order Runge-Kutta method with a temperature step of 0.1°C using a FORTRAN code on a SGI workstation. The sensitivity of the model solution was tested by decreasing the temperature step to 0.01°C, and the simulation was repeated. This test had no effect on the results, thus confirming the convergence of our solution.

Results

Tissue geometry and dimensions

The control histology micrographs were used to measure the Krogh cylinder dimensions (r_{vo} and ΔX). Figure 2 shows the histology of AT-1 tumor tissue. In the micrograph shown, the tumor cells stain dark as compared to the extracellular matrix, and the predominantly white (optically transparent) areas depict vascular channels and the greyish areas represent the interstitial spaces. Stereological measurements on the histology micrographs showed that the vascular channels represent $7 \pm 3\%$, the interstitial areas represent $35 \pm 5\%$ and the total extracellular space represents $42 \pm 8\%$ of the total micrograph area, respectively. A comparable value for the relative volume of interstitial spaces in tumor tissues has been reported by Jain (1987). The distance between the microvascular channels (or the shortest distance between the centers of two AT-1 cells) was measured to be 17.9 ± 2.4 μm, and the initial radius of the extracellular space (r_{vo}) was then determined to be 6.5 ± 1.6 μm, by setting $\pi r_{vo}^2/\Delta X^2 = 0.42$ (see Figures 1 and 2). The axial length of the Krogh cylinder (L) was then found to be 18.1 ± 2.9 μm.

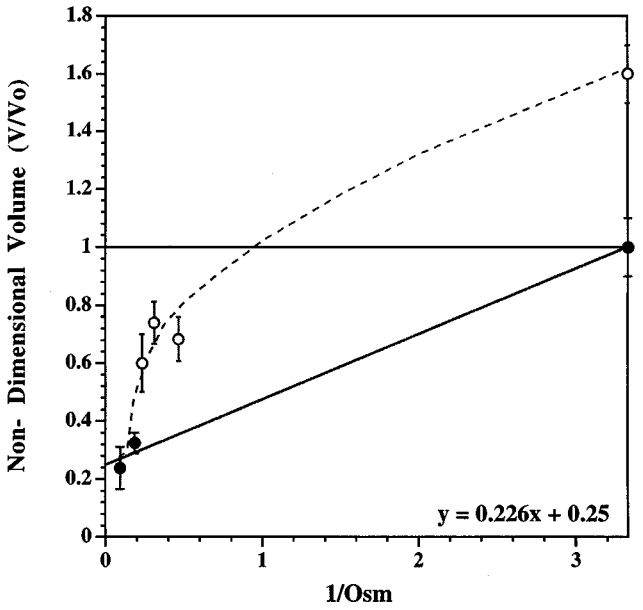

Figure 4. Boyle-van't Hoff plot constructed at constant subzero temperature in the presence of extracellular ice for AT-1 tumor tissue.

The holding temperature was related to the osmolality by the relationship $\text{Osm} = \Delta T/1.858$, where $\Delta T = 273.15 - T$, K. (●) represent the average volumetric data. (——) is a linear curve (assumes the cells behave as ideal osmometers) when extrapolated to infinite osmolality, and results in an osmotically inactive cell volume $V_b = 0.25 V_o$. (– – –) represents the volume of cellular and interstitial components as might be measured by the image analysis technique described in the Materials and Methods section. (○) represent the average volumetric data at temperatures ≥ -8°C, which were not used in predicting the osmotically inactive cell volume V_b because of the effect of interstitial spaces (see Materials and Methods and Results). The inverse of the osmolality is plotted along the *x*-axis and the normalized nondimensional volume is plotted along the *y*-axis. The error bars represent the standard deviation of the data from three separate experiments under identical freezing conditions.

Equilibrium cooling response: estimation of V_b

A Boyle-van't Hoff (BVH) plot was constructed using freeze substituted tissue micrographs of partially dehydrated AT-1 tumor tissue whose cells were equilibrated at different subzero temperatures in the presence of vascular/extracellular ice. The BVH plot (Figure 4) was constructed to estimate the osmotically inactive volume V_b. Each circle (filled and open) represents the average cell volume data from image analysis as previously described. Volumes are normalized to the average cellular volume measured in unfrozen (control) tissue micrographs (histological sections). The error bars represent the standard deviation of the data from three separate experiments under identical freezing conditions. While cellular ma-

terial can be distinguished from interstitium in micrographs of unfrozen tissue, the cellular and interstitial material cannot be distinguished from one another in micrographs of partially-dehydrated tissue. As a result, for temperatures at which interstitial volume is still significant ($-4°$, $-6°$, -8°C in Figure 4; open circles), the cellular volume is overestimated in the image analysis (yielding normalized volumes >1 for slam frozen images). For temperatures at which interstitial volume is negligible ($-10°$ and -20°C in Figure 4; filled circles), the cellular volume is more accurately determined (as described previously in the Materials and Methods section). For this reason, only the $-10°$ and -20°C data points are used to estimate the osmotically inactive cell volume V_b. In Figure 4, the inverse of the osmolality (Osm^{-1}) which the tumor tissue cells experience during freezing is plotted on the x-axis and the normalized equilibrium cell volumes at these osmolalities are plotted on the y-axis. The osmolality was calculated assuming an ideal and dilute extracellular solution; the osmolality can be determined using a Taylor series expansion of the Gibbs-Helmholtz equation as shown by Pitt (1990) and represented as $\mathrm{Osm}^{-1} = 1.858/\Delta T$ (where $\Delta T = 273.15 - T$, K). Linear regression analysis (——) on equilibrium volume data obtained at temperatures of 0°, $-10°$, and -20°C yielded the Boyle-van't Hoff function of $V/V_o = 0.25 + 0.226/\mathrm{Osm}$. The linearity of the plot suggests that the unfrozen AT-1 cells behave as ideal (perfect) osmometers in the presence of extracellular ice; a behavior similar to a variety of biological systems, including isolated AT-1 cells (Smith et al., 1997) and normal rat liver tissue cells (Pazhayannur and Bischof, 1997). By extrapolating to an infinitely concentrated solution, the osmotically inactive cell volume $V_b = 0.25V_o$ is obtained. This value compares quite closely with the value of osmotically inactive cell volume obtained for single, isolated cultured AT-1 cells using a standard cellular cryomicroscopy technique by Smith et al. (1997) and was further corroborated by a stereological analysis of the AT-1 tumor tissue micrographs cooled at 5°C/min to -20°C (shown in Figure 5D), which resulted in an end volume of $0.28V_o$ ($\pm 0.075V_o$). Thus, for the purpose of this study, it was assumed that the osmotically inactive cell volume $V_b = 0.25V_o$.

Dynamic cooling response

Effect of Cooling Rate. Figure 6 shows the cooling rate response in Dunning AT-1 tumor tissue: (A) slam frozen ($>1{,}000$°C/ min; or cooled at (B) 400°C/min; (C) 100°C/min; (D) 50°C/min; (E) 10°C/min; (F) 5°C/min, to an end temperature of -20°C, followed by LN_2 immersion. In Figure 6A, the dark-stained, optically dense areas correspond to the cellular and interstitial components, while the optically transparent areas correspond to the ice crystals that form within the tumor tissue during freezing. Note the gradual increase in the size of ice crystals as the cooling rate decreases. The smaller membrane bounded ice crystals (≤ 15 μm in diameter or less than the size of a single isolated AT-1 cell) are indicative of the formation of intracellular ice (or IIF) and the larger and continuous ice crystals correspond to the water frozen in the extracellular space (due to water transport). The micrographs shown in Figure 6 indicate that IIF occurs in AT-1 tumor tissue cells cooled at the high cooling rate of 400°C/min, while IIF and water transport occur simultaneously at the intermediate cooling rate of 100°C/min and that

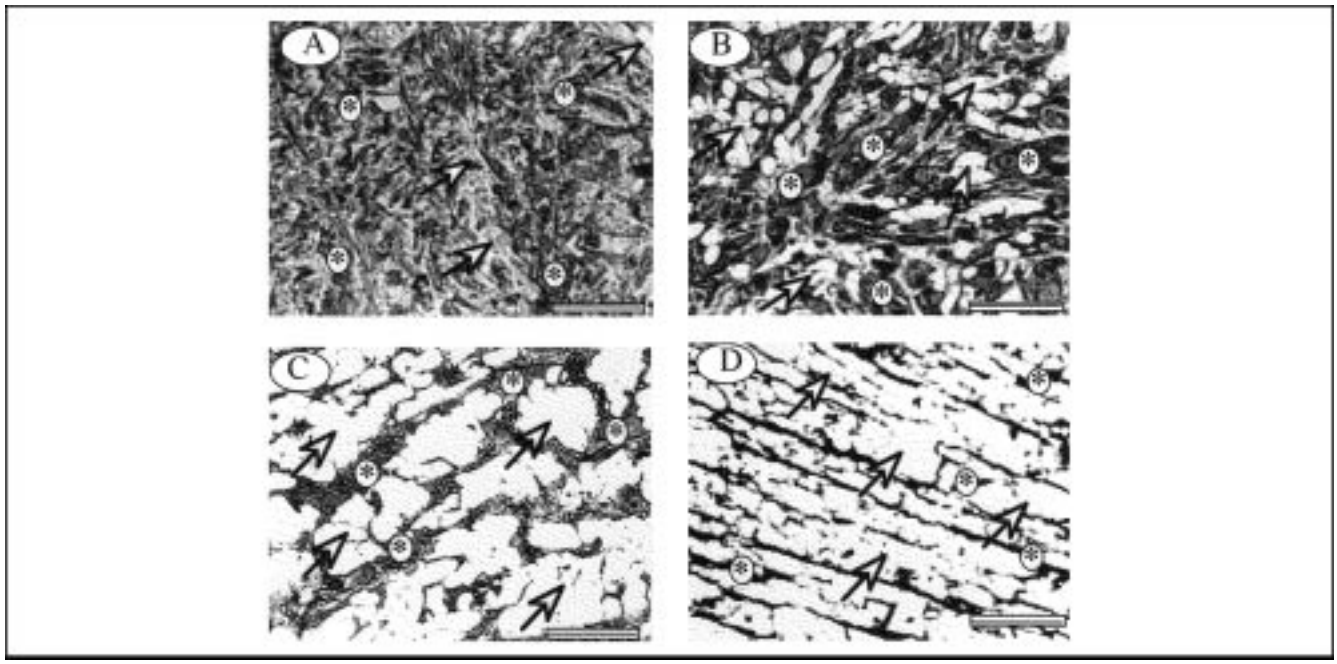

Figure 5. Light micrographs of AT-1 tumor tissue frozen using the two-step freezing process described by Pazhayannur and Bischof (1997).

The first step involved cooling the tissue at 5°C/min on the directional solidification stage to: (A) 0°C; (B) -4°C; (C) -10°C; (D) -20°C followed by a second slam freezing ($>1{,}000$°C/min) step. Dark stained, optically dense areas (represented by stars), correspond to tumor tissue components including the interstitial spaces, while the optically transparent areas (represented by arrows), correspond to the extracellular ice crystals that form within the tumor. (Scale bar = 50 μm.)

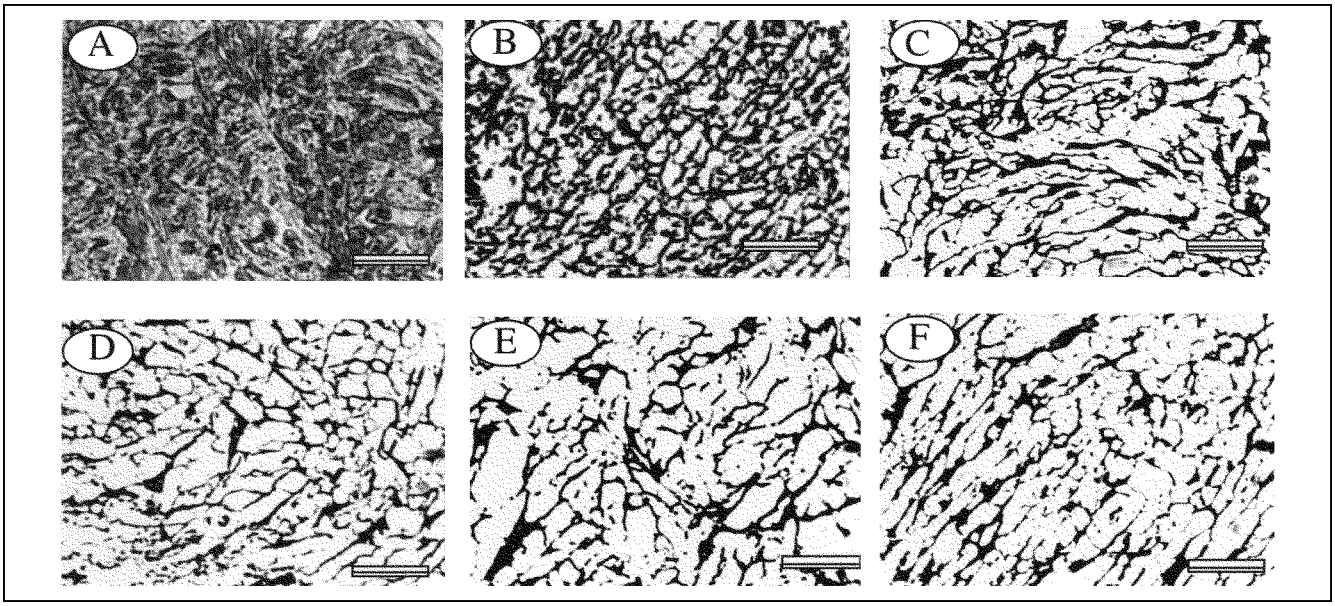

Figure 6. Light micrographs of AT-1 tumor tissue frozen using the two-step freezing process described by Pazhayannur and Bischof (1997).

The micrographs shown were obtained, by cooling the tissue at a cooling rate of (A) slam freezing (> 1,000°C/min); (B) 400°C/min; (C) 100°C/min; (D) 50°C/min; (E) 10°C/min; (F) 5°C/min on the directional solidification stage to −20°C. Dark stained, optically dense areas correspond to tumor tissue components including the interstitial spaces, while the optically transparent areas correspond to the extracellular ice crystals that form within the tumor. (Scale bar = 50 μm.)

water transport is the dominant biophysical response at the lower cooling rates $\leq$ 50°C/min.

Tumor Tissue Cooled at 5°C/min. Figure 5 shows the two-step freezing response in Dunning AT-1 tumor tissue cooled at 5°C/min. The first step involved directional solidification of the tissue at 5°C/min to (B) −4°C, (C) −10°C and (D) −20°C followed by a slam freezing (> 1,000°C/min) step. A tumor sample slam frozen from 2°C is shown in Figure 5A, where the cellular and interstitial components are represented by stars, while the extracellular ice crystals that form within the tumor tissue during freezing are represented by arrows. At −4°C (Figure 5B), alterations in the structure of the tumor tissue are observed. The extracellular region appears enlarged with continuous ice crystals, presumably due to cellular dehydration. A further reduction in temperature to −6°C and −8°C led to greater dehydration of the tumor cells and corresponding expansion of the microvascular channels. The dehydrated AT-1 cells appear to be ''squeezed'' between the expanding ice crystals in the extracellular space. Freezing at 5°C/min down to −10°C (Figure 5C) and further to −20°C (Figure 5D) led to what appears to be total dehydration of the AT-1 cells and formation of large extracellular ice crystals. By performing stereological measurements on micrographs such as in Figure 5, experimental data on volumetric shrinkage during cooling at 5°C/min were obtained (as described earlier in the Materials and Methods section).

DSC and Low-Temperature Microscopy Water Transport Data at 5°C/min. The water transport data and simulation for tumor tissue cells cooled at 5°C/min are shown in Figure 7. The open triangles ($\triangle$) represent DSC data and filled triangles ($\blacktriangle$) represent the low-temperature microscopy data. The dynamic portion of the cooling curve is between −0.53°C to $\sim$ −10°C. The normalized low-temperature microscopy water transport data at −4°C is about 30% greater than the normalized cellular volume predicted by the DSC. We believe this discrepancy between the water transport data obtained using the two techniques is due to the presence of large interstitial spaces introducing an error (or an artifact) in the cellular volumes estimated using the freeze substituted tissue micrographs. [*This result is in contrast to the normal rat liver tissue for which both the DSC and the low-temperature microscopy techniques generate statistically similar water transport data (Devireddy and Bischof, 1998). Note that rat liver tissue consists of < 7.5% interstitial spaces; therefore, the low-temperature microscopy data are presumed unaffected by the artifact of interstitial spaces.*] This difference between the DSC and microscopy water transport data is reduced at lower temperatures, where the interstitial spaces collapse substantially (as discussed previously in the Materials and Methods section) during the freezing process. The best fit membrane permeability parameters of water transport to the 5°C/min DSC and low-temperature microscopy volumetric shrinkage data were: $L_{pg} = 1.0 \times 10^{-13}$ m^3/N·s (0.6 μm/min·atm) and E_{Lp} = 282.9 kJ/mol (67.6 kcal/mol), and $L_{pg} = 0.14 \times 10^{-13}$ m^3/N·s (0.08 μm/min-atm) and $E_{Lp} = 77.30$ kJ/mol (18.5 kcal/mol), respectively (see Table 1). The parameters generated from the DSC data are taken to be the more physically realistic of the two cases due to the effect of the interstitial error in the low-temperature microscopy data. The volumetric response generated by these parameters in Eq. 6 are shown in Figure 7 as solid lines (——). The model predicted equilibrium cooling response (cells cooled infinitely slowly) is also shown for reference as a dashed line (– – –).

DSC Water Transport Data at Higher Cooling Rates (10° and 20°C/min). The water transport data and simulation for tumor tissue cells cooled at 10° and 20°C/min are shown in

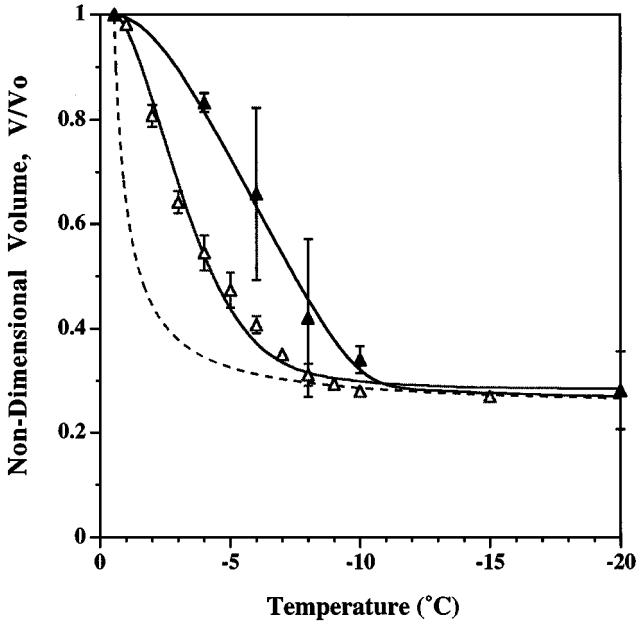

Figure 7. Volumetric response of AT-1 tumor tissue as a function of subzero temperatures using the low-temperature microscopy method and the DSC technique at 5°C/min.

(△) and (▲) represent the 5°C/min DSC and low-temperature microscopy water transport data, respectively. The error due to interstitial spaces in the low-temperature microscopy water transport data causes it to be consistently higher than the DSC water transport data. The Krogh model simulated response using the predicted membrane permeability parameters (from the DSC and low-temperature microscopy 5°C/min water transport data) in Eqs. 6 and 7 are also shown (——). The Krogh model simulated equilibrium cooling response obtained assuming $V_b = 0.25V_o$ and $dV/dT = 0$ in Eq. 6, is shown as (– – –). The nondimensional volume is plotted along the *y*-axis and the subzero temperatures are shown along the *x*-axis. The error bars represent the standard deviations in the data ($n = 3$ for low-temperature microscopy data and $n = 6$ for DSC data).

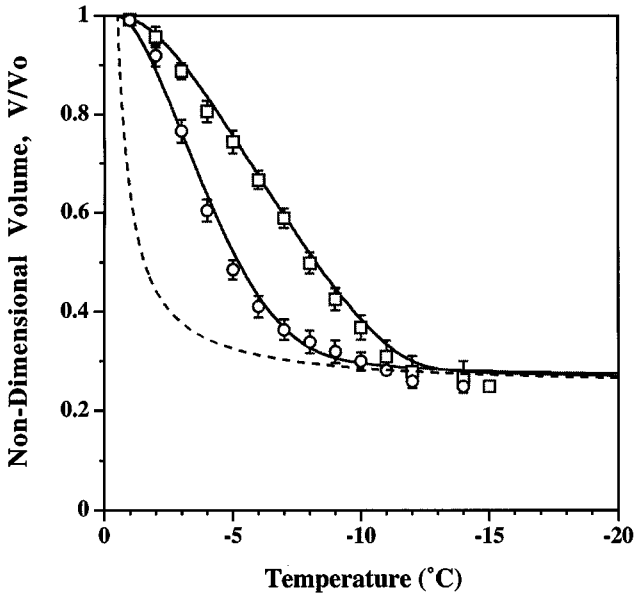

Figure 8. Volumetric response of AT-1 tumor tissue as a function of subzero temperatures obtained using the DSC technique at cooling rates of 10° and 20°C/min.

(○) and (□) represent the 10° and 20°C/min DSC water transport data, respectively. The Krogh model simulated response using the predicted membrane permeability parameters (from the DSC 10° and 20°C/min water transport data) in Eqs. 1 and 2 are also shown (——). The Krogh model simulated equilibrium cooling response obtained assuming $V_b = 0.25V_o$ and $dV/dT = 0$ in Eq. 6, is shown as (– – –). The nondimensional volume is plotted along the *y*-axis and the subzero temperatures are shown along the *x*-axis. The error bars represent the standard deviations in the data ($n = 6$).

Figure 8. The open circles (○) and open squares (□) represent the 10° and 20°C/min DSC water transport data. The dynamic portion of the cooling curve is between −0.53°C to ~ −12°C and between −0.53°C and −15°C for the cooling rates of 10° and 20°C/min, respectively. The best fit parameters of Eq. 6 to the DSC 10° and 20°C/min water transport data, using the Krogh model are shown in Table 1. These parameters were: $L_{pg} = 1.08 \times 10^{-13}$ m^3/N·s (0.65 μm/min·atm) and $E_{Lp} = 213.0$ kJ/mol (50.9 kcal/mol) at 10°C/min, while the 20°C/min DSC water transport data yielded the values: $L_{pg} = 0.67 \times 10^{-13}$ m^3/N·s (0.4 μm/min·atm) and $E_{Lp} = 95.8$ kJ/mol (22.9 kcal/mol). The cell volume predictions generated by these two parameter pairs are shown in Figure 8 as solid lines (——) and the model predicted equilibrium cooling response is also shown (– – –).

There is a significant decrease (~ 50%) in the predicted value of membrane reference permeability L_{pg} and the activation energy E_{Lp} between the 10° and 20°C/min DSC water transport data. It might be that the AT-1 tissue cells cooled at 20°C/min undergo incomplete dehydration and the final end volume is significantly higher ($> 0.5\ V_o$) than the osmotically inactive cell volume of 0.25 V_o. This would lead to an incorrect estimation of the water transport data on the basis of Eq. 9, which results in an incorrect estimation of the membrane permeability parameters. To test this possibility, light micrographs of AT-1 tumor tissue, cooled at even higher rates where more incomplete water transport would be noticed, were examined. Tissue cooled at 50°C/min to −90°C (taken

Table 1. Membrane Permeability Parameters for Dunning AT-1 Rat Prostate Tumor Tissue Assuming a Krogh Model*

Experimental Technique	Cooling Rate	L_{pg} $10^{13} \times$ m^3/N·s (μm/min·atm)	E_{Lp} kJ/mol (kcal/mol)	R^2 Value
Low-Temperature Microscopy Method	5°C/min	0.14 (0.08)	77.30 (18.5)	0.99
DSC Technique	5°C/min	1.00 (0.60)	282.9 (67.6)	0.99
	10°C/min	1.08 (0.65)	213.0 (50.9)	0.98
	20°C/min	0.67 (0.40)	95.8 (22.9)	0.99
	Combined Best Fit**	0.60 (0.36)	100.4 (24.0)	0.99

*A tabulated comparison of the membrane permeability parameters obtained using the DSC water transport data at 5°, 10° and 20°C/min and using the low-temperature microscopy water transport data at a cooling rate of 5°C/min assuming a Krogh cylinder geometry (see Figure 1).

**The combined best fit parameters minimized the R^2 value at all the three cooling rates.

from a previous study by Bischof et al., 1997) and at 50°C/min to −20°C (obtained in this study) were analyzed for possible evidence of shift to incomplete water transport or a shift to IIF from water transport. Figure 6D shows a light micrograph of AT-1 tumor tissue cooled at 50°C/min to −20°C with a stereologically measured cellular end volume of $0.43V_o$ ($\pm 0.05V_o$), which further decreases to $0.3V_o$ ($\pm 0.05V_o$) at an end temperature of −90°C (Bischof et al., 1997). These data suggest that water transport is still the dominant biophysical response even at 50°C/min. Therefore, a cooling rate of 20°C/min should predominantly cause water transport or cellular dehydration in AT-1 tumor tissue slices, and the change in the membrane permeability parameters is likely not due to a shift in the biophysical response to IIF but may be intrinsic to the water transport data itself where more information is contained in data from cooling rates further away from equilibrium cooling (see discussion).

Numerical simulations

Numerical simulations were performed at various cooling rates (5°−100°C/min) using a Krogh cylinder model and the combined best fit parameters in Eq. 6. The combined best fit membrane permeability parameters maximized the goodness of the fit parameter R^2 for the DSC 5°, 10°, and 20°C/min water transport data concurrently and were found using the nonlinear curve fitting technique described earlier. Thus, a new set of membrane permeability parameters was obtained that produce a combined best fit to the experimentally determined water transport data at three different cooling rates (5°, 10°, and 20°C/min), that is, $L_{pg} = 0.6 \times 10^{-13}$ m^3/N·s (0.36 μm/min·atm) and $E_{Lp} = 100.4$ kJ/mol (24.0 kcal/mol). Simulations of the volumetric behavior of AT-1 tumor tissue cells using these combined best fit parameters are shown for a variety of cooling rates in Figure 9. Two different variables are graphed against temperature: (1) the nondimensional cellular volume (V/V_o), which decreases due to dehydration during freezing; (2) the nondimensional radius (μm) of the extracellular space (r_v/r_{vo}), which expands during freezing. The Krogh model simulations show that AT-1 tumor tissue cells cooled at rates $\leq$ 50°C/min are essentially dehydrated (once cooling has proceeded to temperatures < -20°C), however, at rates $>$ 50°C/min, the amount of water trapped within the tissue cells increases rapidly with increasing cooling rates. The results were analyzed to predict the end cell volume at various cooling rates (that is, the amount of water left in the tumor tissue cell) and the radius of the extracellular space after dehydration ceases.

From the simulations, the amount of trapped water (or intracellular ice volume, IIV) was computed as a ratio of the volume of the water trapped inside the tissue cell at the temperature where water transport ceases ($T < -30$°C) to the initial tissue water volume, $[(V_e - V_b)/(V_o - V_b)]$, as described

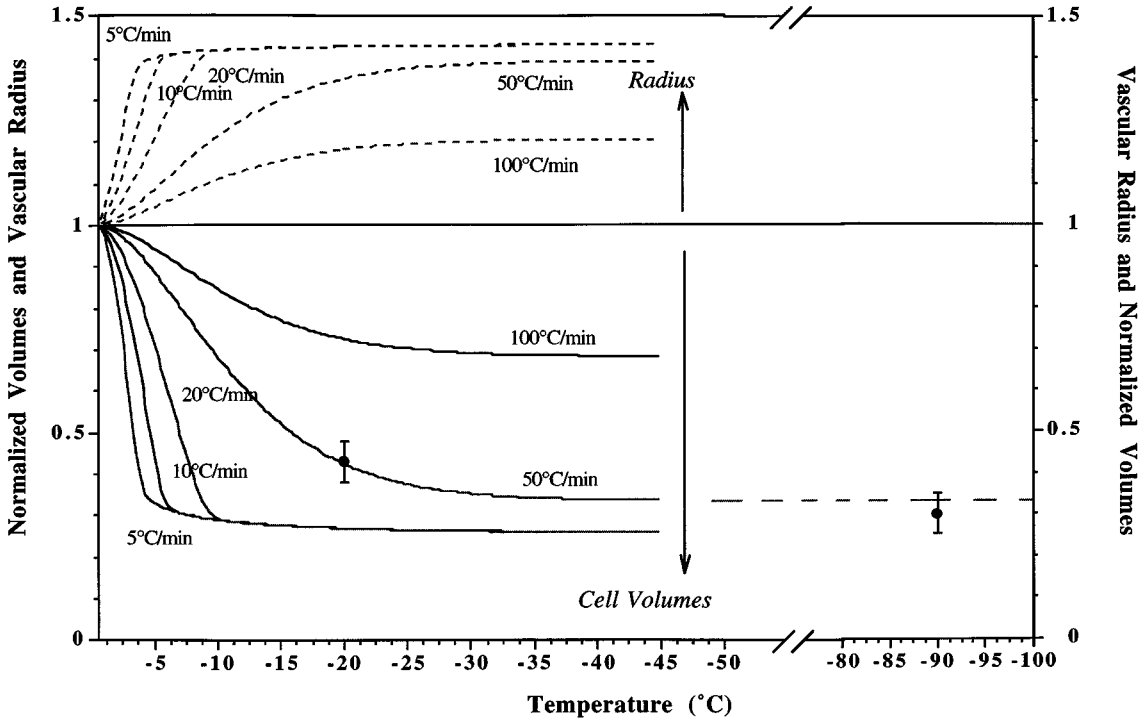

Figure 9. Krogh model: Volumetric response of AT-1 tumor tissue at various cooling rates as a function of subzero temperatures using the combined best fit membrane permeability parameters (see Table 1).

Lower Graph: Changes in the normalized volume of the Krogh model as a function of temperature for different cooling rates (5°, 10°, 20°, 50°, and 100°C/min). Krogh cell volume (——). The measured end volumes from light micrographs cooled at 50°C/min to −20°C and −90°C are shown as (●) and the error bars represent the standard deviation in the data ($n = 3$). *Upper Graph:* Changes in the normalized radius of the extracellular space (r_v/r_{vo}) of the vasculature in the Krogh unit as a function of temperature for different cooling rates. The normalized radius of the extracellular space is also given as (− − −). The subzero temperatures are shown along the *x*-axis.

earlier by Pazhayannur and Bischof (1997). [*Where V_e is the end volume after water transport ceases (at ~ -20°C), and V_o and V_b are the initial (isotonic) and final (osmotically inactive) tumor cell volumes, respectively.*] On further cooling, this trapped water will change to ice with sufficient supercooling. For cooling rates of ≤ 20°, 50°, and 100°C/min, the trapped water volume was 2.7%, 22.7%, and 62.7% of initial intracellular water volume, respectively, and the corresponding end volumes were 0.27, 0.42, and $0.72V_o$, respectively. The experimentally determined end volumes at -20°C and -90°C for the cooling rate of 50°C/min are also shown on the graph as (●) and are found to be in close agreement with the numerically predicted end volumes. If intracellular ice formation occurs prior to the completion of water transport (which our model does not predict), then the end volume will be even higher. Note that, as cells dehydrate, the vascular/extracellular volume will increase along with the radius of the extracellular space. For cooling rates of ≤ 20°, 50°, and 100°C/min, the numerically predicted value of the radius of the extracellular space at -20°C were 9.3, 8.8, and 7.7 μm, respectively, and the corresponding values of the nondimensional radius of the extracellular space (r_v/r_{vo}) were 1.43, 1.35, and 1.18, respectively.

Spherical cell model: effect of varying membrane surface area (A_c)

To study the effect of varying the cell membrane surface (A_c) on the predicted membrane permeability parameters (L_{pg} and E_{Lp}), it was assumed that the AT-1 tumor tissue cells behave as isolated AT-1 spherical cells (with a diameter of 18.7 μm, Smith et al., 1997) embedded in an extracellular matrix. A spherical cell model represents an extreme of a Krogh model where cell-cell contact is neglected and the cell membrane surface area through which water transport occurs is the maximum possible value: A_c is $\sim$1,099 μm^2 assuming a spherical cell model as opposed to $\sim$739.5 μm^2 in the Krogh model (shown in Figure 1). The best fit membrane permeability parameters of water transport to the 5°C/min DSC and low-temperature microscopy volumetric shrinkage data using the spherical cell model were: $L_{pg} = 0.58 \times 10^{-13}$ m^3/N·s (0.35 μm/min·atm) and $E_{Lp} = 207.2$ kJ/mol (49.5 kcal/mol), and $L_{pg} = 0.067 \times 10^{-13}$ m^3/N·s (0.04 μm/min·atm) and $E_{Lp} = 18.8$ kJ/mol (4.5 kcal/mol), respectively (see Table 2). The combined best fit membrane permeability parameters for the DSC 5, 10 and 20°C/min water transport data using the spherical cell model were predicted to be: $L_{pg} = 0.5 \times 10^{-13}$ m^3/N·s (0.3 μm/min·atm) and $E_{Lp} = 96.3$ kJ/mol (23.0 kcal/mol).

Table 2. Membrane Permeability Parameters for Dunning AT-1 Rat Prostate Tumor Tissue Assuming a Spherical Cell Geometry*

Experimental Technique	Cooling Rate	L_{pg} $10^{13} \times$ m^3/N·s (μm/min·atm)	E_{Lp} kJ/mol (kcal/mol)	R^2 Value
Low-Temperature Microscopy Method	5°C/min	0.067 (0.04)	18.8 (4.50)	0.99
DSC Technique	5°C/min	0.58 (0.35)	207.2 (49.5)	0.99
	10°C/min	0.70 (0.40)	177.0 (42.3)	0.99
	20°C/min	0.50 (0.30)	95.4 (22.8)	0.99
	Combined Best Fit**	0.50 (0.30)	96.3 (23.0)	0.99

*A tabulated comparison of the membrane permeability parameters obtained using the DSC water transport data at 5°, 10° and 20°C/min and using the low-temperature microscopy water transport data at a cooling rate of 5°C/min assuming a spherical cell geometry (with a diameter of 18.7 μm).

**The combined best fit parameters minimized the R^2 value at all the three cooling rates.

Discussion

Comparison of the two techniques

The DSC technique has several advantages and disadvantages when compared with the low-temperature microscopy method of Pazhayannur and Bischof (1997). Perhaps, the chief advantage of the DSC technique is its ability to generate continuous dynamic water transport response data while the microscopy methods (either histology or freeze substitution techniques) are ideally suited to measure the initial Krogh cylinder dimensions and the final osmotically inactive volumes of tumor tissue cells, exposed to a specified cooling rate or freezing protocol. Other advantages of the DSC technique are that it is faster and less labor intensive. Since the DSC water transport data is a volume-averaged response over a large sample of tissue (that is, a macroscopic response as opposed to a microscopic cell level response obtained with the low-temperature microscopy technique), the effect of intratumor deviations in transport behavior is minimized. Consequently, the DSC water transport data has smaller standard deviations.

This study has also shown that the low-temperature microscopy method is not well suited to measure water transport in tumor tissue systems. Tumor tissue systems are characterized by the presence of large interstitial spaces (Jain, 1987), which we believe introduces an error in the estimation of cellular volumes using the low-temperature microscopy method. The DSC technique is ideally suited to measure water transport in tumor tissue systems, as it is unaffected by the presence of interstitial spaces. Perhaps, the two biggest disadvantages of the DSC technique are: (a) that it cannot distinguish between the heat released due to dehydration (water transport) and intracellular ice formation (IIF); (b) that it requires the initial (V_o and Krogh model dimensions) and the final osmotically inactive cell volume (V_b). Therefore, the low-temperature microscopy method is essential to determine a qualitative difference between water transport and IIF during freezing of tumor tissue cells at various controlled cooling rates and in obtaining the initial and final cell volumes. Another disadvantage of the DSC is that it cannot be used for cooling rates ≥ 40°C/min, since at these high cooling rates, the DSC heat release measurement becomes unreliable (Devireddy and Bischof, 1998). Thus, this study defines how the DSC technique and the microscopy methods (histology and the two-step freezing method described by Pazhayannur and Bischof, 1997) can be used together to measure water transport response of tumor tissue cells during freezing. It is suggested that the histology and low-temperature microscopy method be used to measure the static (initial and final) cell volumes for a given cooling rate and the DSC method is used to measure how the cell volume changes dynamically from its initial to final volume during freezing.

Parameter sensitivity analysis

Effect of Varying Cell Membrane Surface Area (A_c). The membrane permeability parameters obtained using the spherical cell model (shown in Table 2) are uniformly lower than those obtained using the Krogh model (shown in Table 1). A closer inspection of the predicted best fit membrane permeability parameters obtained using the Krogh and spherical cell model shows that the decrease in L_{pg} is more significant than the decrease in E_{Lp}. For example, at 5°C/min L_{pg} decreases by $\sim 41\%$ between the Krogh and spherical cell model while E_{Lp} decreases by only 26%. This decrease in the predicted membrane permeability parameters between the Krogh and the spherical cell model is not surprising, since Eq. 6 shows that the change in the tissue cell volume as a function of temperature (dV/dT) is proportional to the product of L_p and A_c. Thus, for a given change in the tissue cell volume as a function of temperature (dV/dT), an increase in A_c will cause a corresponding decrease in the predicted value of L_p, where $L_p = f(L_{pg}, E_{Lp})$ as shown in Eq. 7. Thus, any changes to the geometrical model of the tissue cell (specifically membrane surface area A_c) should manifest themselves with corresponding changes to the model predicted membrane permeability parameters (L_{pg} and E_{Lp}).

Numerical simulations were performed assuming a spherical cell model and using the combined best fit parameters (shown in Table 2) in the water transport model (Eqs. 6 and 7). The predicted end volumes for a cooling rate of 50°C/min to -20°C using the spherical cell model was $0.42V_o$ and agrees quite closely with the experimentally determined end volume of $0.43V_o$ ($\pm 0.05V_o$) (see Results, Figure 6D and Figure 9). This suggests that it might be appropriate to model the AT-1 tumor tissue cells as individual spherical cells embedded in an extracellular matrix, since the presence of large interstitial spaces reduces the cell-cell contact in AT-1 tumor tissue slices. So, both the Krogh model (which has been adequately shown in the Results) and the spherical cell model can be used to model the mass transfer during freezing of the AT-1 tumor tissue cells. However, the Krogh model captures the physical morphology of the tissue system more accurately than the spherical cell model, by assigning finite dimensions to the extracellular/vascular spaces. Thus, it is suggested that the modified Krogh model (shown in Figure 1), which accounts for the presence of large interstitial spaces and which also assumes a finite vascular/extracellular space, be used to model the AT-1 tumor tissue cells.

Effect of Varying the Osmotically Inactive Cell Volume (V_b). To study the effect of varying the osmotically inactive cell volume on the predicted membrane permeability parameters (L_{pg} and E_{Lp}), the value of V_b was varied from $0.125V_o$ to $0.375V_o$ (that is, 50% variation in the measured value of $0.25V_o$, see Figure 4). The DSC data was correspondingly modified (using Eq. 9) and the modified DSC water transport data was curve fitted to the water transport model (Eqs. 6 and 7) using the nonlinear least-squares curve fitting technique as previously described. The predicted values of the membrane permeability parameters (L_{pg} and E_{Lp}) using $0.125V_o$ and $0.375V_o$ as the osmotically inactive cell volume were found to be within 20% of the values obtained using an osmotically inactive cell volume of $0.25V_o$. Pazhayannur and Bischof (1997) and Devireddy et al. (1998) also note a similar lack of sensitivity of the membrane permeability parameters to the value of the osmotically inactive cell volume in rat liver tissue and human lymphocyte cells, respectively. Thus, errors in the estimated value of V_b using the BVH plot (Figure 4) can alter the model predicted membrane permeability parameters (shown in Tables 1 and 2), but the trends remain the same.

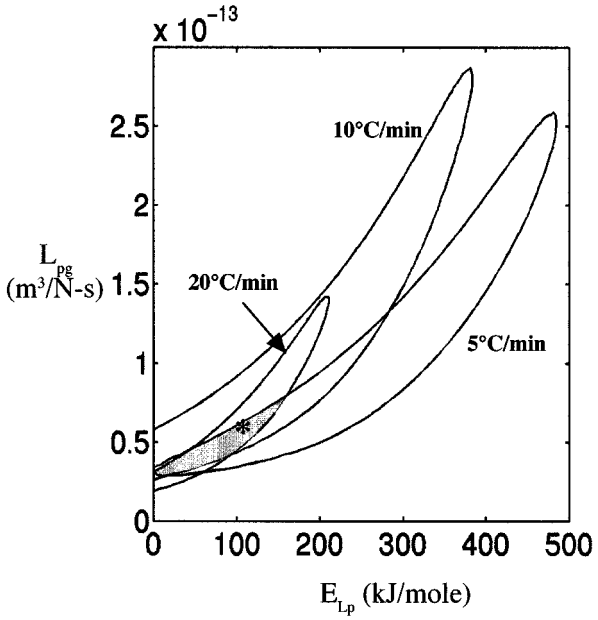

Figure 10. Contour plots of the goodness of fit parameter R^2 (= 0.95) for water transport response in Dunning AT-1 tumor tissue.

The predicted combined best fit parameters for all the three cooling rates $L_{pg} = 0.6 \times 10^{-13}$ m³/N·s (0.36 μm/min·atm) and $E_{Lp} = 100.4$ kJ/mol (24.0 kcal/mol) are also shown (*). The shaded region corresponds to the range of parameters that fit the water transport data at all the three cooling rates. The membrane permeability at 0°C, L_{pg} (m³/N·s) is plotted on the *y*-axis while the apparent activation energy of the membrane, E_{Lp} (kJ/mol) is plotted on the *x*-axis.

Effect of Varying the Cooling Rate. The combined best fit membrane permeability parameters of water transport for AT-1 prostate tumor tissue compare well with the parameters obtained at the higher cooling rate of 20°C/min (see Table 1). Figure 10 shows a contour plot of the goodness of fit parameter R^2 in the L_{pg} and E_{Lp} space that fits the DSC water transport data at the three cooling rates. Any combination of L_{pg} and E_{Lp} shown to be within the contour will fit the water transport data at that cooling rate with an R^2 value > 0.95. Note that the $R^2 = 0.95$ contour for the 20°C/min lies within the corresponding contours for the 5° and 10°C/min. The predicted best fit parameters are denoted by a star (*) and fall within all the three contours. This suggests that the membrane permeability parameters obtained using the 20°C/min water transport data could predict the volumetric response of the tumor tissue at 5° and 10°C/min quite accurately, while the converse is not true. This might be due to the fact that the 20°C/min water transport data is farther away from equilibrium (that is, it contains more dynamic information) than the 5° and 10°C/min water transport data.

This implies that to obtain the membrane permeability parameters of water transport that best predict the behavior of a biological system, water transport data needs to be obtained at the highest possible cooling rate at which dehydration occurs exclusively. Smith et al. (1998) also report a similar behavior (that is, higher cooling rate parameters are better able to predict the lower cooling rate water transport response than vice versa) in isolated rat (male, Sprague-Dawley) hepatocytes.

Comparison of cell and tissue level parameters

The parameters predicted for the AT-1 tumor tissue in this study are compared to those reported in previous single cell studies. The Dunning AT-1 tumor tissue parameters measured in this study are *not in agreement* with reported values for single, isolated cultured AT-1 cells obtained using a standard cellular cryomicroscopy technique by Smith et al. (1997): $L_{pg} = 4.46 \times 10^{-13}$ m^3/N·s (2.71 μm/min·atm), and $E_{Lp} =$ 232 kJ/mol (55.4 kcal/mol). This is in contrast with the rat liver tissue system where the membrane permeability parameters for isolated, cultured, and digested hepatocyte cells (Yarmush et al., 1992) and for rat liver tissue cells (Pazhayannur and Bischof, 1997; Devireddy and Bischof, 1998) were found to be in good agreement. The AT-1 cell level study reported by Smith et al. (1997) was performed on AT-1 cells cultured *in vitro* as described by Bischof et al. (1997). To obtain the isolated AT-1 cell suspensions, trypsin was used to detach the AT-1 cells from the T-flask. A study is currently underway in our lab to examine the effects of trypsin on the AT-1 cell behavior during freezing, and preliminary results show that the amount of trypsin used can have a dramatic impact on the cell freezing behavior. Other differences also exist between the cell and tissue level studies that might account for the measured differences in membrane permeabilities: (a) effect of tumor cells embedded in a extracellular vascular space (finite extracellular space) in the tissue system as opposed to tumor cells suspended in a solution (infinite extracellular space); (b) alterations in the membrane properties of the tumor tissue cells which are grown in the hind limb of a Copenhagen rat vs. tumor cells cultured in a T-flask.

Mechanism(s) of mass transfer through biological membranes

The water transport permeability parameters (L_{pg} and E_{Lp}) reported in this study (see Tables 1 and 2) are within the range of the reported values for many mammalian cells, which have typical values ranging from $L_{pg} = 0.16$ to 1.65×10^{-13} m^3/N·s (0.01 to 1.0 μm/min·atm) and $E_{Lp} = 21$ to 84 kJ/mol (5 to 20 kcal/mol) (see McGrath, 1988, for a comprehensive review). The activation energies presented in this study are greater than the activation energy for self-diffusion of water ($\sim$16.7 kJ/mol or 4 kcal/mol), which suggests that the water permeation across the cell membrane is through an unfacilitated, passive transport of water molecules, probably through the lipid phase of the membrane. By applying a mechanistic reaction rate theory, Levin et al. (1976) showed that the two limiting cases for water permeation through a homogeneous membrane during freezing are either the diffusion of water within the membrane (diffusion rate-limited) or the passage of water across the solution-membrane interfaces (absorption rate-limited). Levin et al. (1976) also presented an intermediate rate limiting process which they call surface rate-limited; this process does not possess a unique value for activation energy and varies over the temperature range of interest. Distinguishing between the two limiting mechanisms of water permeation (either diffusion rate-limited or absorption rate-limited) is possible only after determining the membrane thickness and the dependence of membrane permeability on the partition coefficient (K_m, defined as the ratio of rate constants for passage of water through the solution and the membrane). Unfortunately, these values are not readily available for most cellular and tissue membranes. Thus, the water permeability parameters obtained in this study do not allow us to relate to a specific mechanism of water transport across the cell membrane.

Implications for cryosurgery

The cooling rates used in the numerical simulations shown in Figure 9 correspond to those typical of various positions within the cryo-iceball. The temperature profiles experienced in a cryo-iceball and the extent of an iceball (as a function of time) are reported in the literature by many investigators. A partial list of work in this area includes the classical and approximate solutions by Cooper and Trezek (1972) and the solutions obtained using finite-element (Comini and Del Guidice, 1976; Budman et al., 1986) and finite-difference methods (Bischof et al., 1997; Rabin and Shitzer, 1998). In general, during cryosurgery two main areas of freezing occur: (a) an area near the probe tip where the freezing rates are rapid (50° to 100°C/min) and the end temperatures are very low, < -100°C; (b) the majority of cryo-iceball which experiences cooling rates < 50°C/min and relatively high end temperatures of > -40°C.

The membrane permeability parameters of water transport obtained in the present study show that the majority of the AT-1 tumor cells in the cryolesion undergo various degrees of cellular dehydration, apart from the tumor cells very near the probe tip (cooling rates > 100°C/min) which probably experience intracellular ice formation (IIF). Roberts et al. (1997) showed that AT-1 tumor tissue samples treated *in vitro* with controlled thermal histories, 50°C/min to -90°C and 35°C/min to -75°C (followed immediately by rapid thawing and after 7 days incubation in culture media at 37°C) exhibit total destruction. At these cooling rates, the simulations in Figure 9 show that these AT-1 tumor cells experience incomplete dehydration; therefore, the lethal freezing injury is probably due to some effect other than IIF, perhaps a mechanism related to the low end temperatures < -60°C experienced by these cells (Marcove, 1972). A strong dependence of cell viability on end temperature has also been observed in Walker carcinoma cells (Jacob et al., 1985) and in human prostate cancer cells (Tatsutani et al., 1996).

Roberts et al. (1997) also showed that AT-1 tissue samples treated *in vitro* with controlled thermal histories indicative of those experienced by the majority of the cells, that is, 10°C/min to -40°C and 5°C/min to -20°C (followed immediately by rapid thawing and after 7 days incubation in culture media at 37°C) exhibit marginal to significant survival, respectively. At these cooling rates (1–10°C/min), the simula-

tions in Figure 9 show that the tumor cells experience extreme dehydration and a consequent expansion of the vascular channels (2 to 3 times), leading to vascular distension. Vascular distension could damage the vascular walls sufficiently to cause stasis, leading to ischemic necrosis in the cryotreated area (Rabb, 1974). The adverse effect of vascular distension (and injury to vascular channels) on tumor tissue viability could then account for the size of the cryolesion being much closer to the size of the original iceball, as suggested in some *in vivo* studies (Neel et al., 1971). Further work on defining the precise impact of both the cellular and vascular injury mechanisms during cryosurgery is clearly warranted.

Conclusion

This study presents water transport data during freezing of Dunning AT-1 rat prostate tumor tissue cells using two different techniques at various cooling rates. Histology of control tumor tissue and a low-temperature microscopy method were used to generate the initial (V_o) and final (V_b) end volumes of the tumor cells, respectively. The tumor tissue was modeled geometrically using a Krogh cylinder model. The initial dimensions of the Krogh cylinder model ($r_{vo} = 6.5\ \mu$m, $\Delta X = 17.9\ \mu$m and $L = 18.1\ \mu$m) were obtained by stereological analysis of control histology of tumor tissue. By constructing a Boyle-van't Hoff plot, an osmotically inactive cell volume V_b of $0.25V_o$ was obtained. A comparison of the 5°C/min DSC and low-temperature microscopy water transport data showed that the microscopy data had a significant error due to the artifact of interstitial spaces on the image analysis technique used. On the other hand, the DSC technique can only be used when the initial and final volumes of the tissue are known and histology and low-temperature microscopy methods are ideally suited to measure these quantities. A Krogh model of water transport was fit to the DSC 5°, 10° and 20°C/min water transport data and the combined best fit membrane permeability parameters of water transport were obtained using a nonlinear curve fit to obtain: reference membrane permeability of the AT-1 tumor tissue cells $L_{pg} = 0.6\times10^{-13}$ m^3/N·s (0.36 μm/min·atm) and the apparent activation energy of the membrane permeability $E_{Lp} = 100.4$ kJ/mol (24.0 kcal/mol). Numerical simulations were performed using the Krogh model and the combined best fit parameters. The simulations were analyzed to predict the amount of intracellular water trapped after water transport ceases and the radius of the extracellular space (r_{vo}) at various cooling rates (5°−100°C/min). The simulations and experimental data were found to be in good agreement and suggest that AT-1 tumor tissue cells experience predominantly cellular dehydration when cooled < 50°C/min, which corresponds to rates experienced in a majority of cryosurgical iceballs.

Acknowledgments

This work was supported by NSF-CTS No. 9410004 and NSF-BES No. 9703326 and a grant from Whitaker Foundation to J. B. Special thanks to Parasuram Pazhayannur for his help with the low-temperature microscopy experiments. Acknowledgments are also due to the Dept. of Chemical Engineering, University of Minnesota, in particular to Dr. Chris Macosko for access and to Dr. David Giles for his help with the DSC-7 machine.

Notation

C_i = initial cell osmolality, 0.285 mol/kg H_2O
q = energy of heat release, a function of temperature, mJ/mg
ρ = density, kg/m^3
r = radius of isolated AT-1 cells, 9.35 μm
R = universal gas constant, 8.314 J/mol K (8.02×10^{13} μm^3·atm/mol K)
v_w = molar volume of water, 18×10^{12} μm^3/mol
Δq_{dsc} = measured difference in DSC heat release in the dynamic cooling protocol, function of temperature, J/g total sample

Subscripts

$ec + cw$ = vascular/extracellular space occupied by media (PBS) with *P. syringae* + tissue cellular water (intracellular fluid), mg
$ec + cw + cd$ = vascular/extracellular space (media) + tissue cell water and cell debris (osmotically inactive tissue cells) with *P. syringae*, mg

Literature Cited

American Cancer Society, "Cancer Facts and Figures," p. 13 (1996).
Bert, J. L., and R. H. Pearce, "The Interstitium and Microvascular Exchange," *Handbook of Physiology—The Cardiovascular System*, E. M. Renkin and C. C. Michel, eds., Vol. 4, Chap. 12, American Physiological Society, Bethesda, MD (1984).
Bevington, P. R., and D. K. Robinson, *Data Reduction and Error Analysis for the Physical Sciences*, 2nd ed., McGraw-Hill, New York (1992).
Bischof, J. C., K. Christov, and B. Rubinsky, "A Morphological Study of Cooling Rate Response in Normal and Neoplastic Human Liver Tissue: Cryosurgical Implications," *Cryobiology*, **30**, 482 (1993).
Bischof, J. C., D. J. Smith, P. V. Pazhayannur, C. Manivel, J. Hulbert, and K. P. Roberts, "Cryosurgery of Dunning AT-1 Rat Prostate Tumor: Thermal, Biophysical and Viability Response at the Cellular and Tissue Level," *Cryobiology*, **34**, 42 (1997).
Budman, H., A. Shitzer, and D. Del Guidice, "Investigation of Temperature Fields Around Embedded Cryoprobes," *ASME J. of Biomech. Eng.*, **108**, 42 (1986).
Comini, G., and S. Del Guidice, "Thermal Aspects of Cryosurgery," *ASME J. of Heat Transfer*, **98**, 543 (1976).
Cooper, T. E., and G. J. Trezek, "On the Freezing of Tissue," *ASME J. of Heat Transfer*, **94**, 251 (1972).
Devireddy, R. V., D. Raha, and J. C. Bischof, "Measurement of Water Transport During Freezing in Cell Suspensions Using a Differential Scanning Calorimeter," *Cryobiology*, **36**(2), 124 (1998).
Devireddy, R. V., and J. C. Bischof, "Measurement of Water Transport During Freezing in Mammalian Liver Tissue—Part II: The Use of Differential Scanning Calorimetry," *ASME J. of Biomech. Eng.*, **120**(5), 559 (1998).
Diller, K. R., "Quantitative Low Temperature Optical Microscopy of Biological Systems," *J. Microscopy*, **126**, 9 (1982).
Echlin, P., *Low Temperature Microscopy and Analysis*, Chapters 3 and 7, Plenum Press, New York (1992).
Hua, T. C., E. G. Cravalho, and L. Jiang, "The Temperature Difference across the Cell Membrane during Freezing and its Effect on Water Transport," *Cryo-Letters*, **3**, 255 (1982).
Jain, R. K., "Transport of Molecules in the Tumor Interstitium: A Review," *Cancer Res.*, **47**, 3039 (1987).
Jacob, G., M. N. Kurzer, and B. J. Fuller, "An Assessment of Tumor Cell Viability after *in vitro* Freezing," *Cryobiology*, **22**, 417 (1985).
Körber, C. H., S. Englich, and G. Rat, "Intracellular Ice Formation: Cryomicroscopical Observation and Calorimetric Measurement," *J. Microscopy*, **161**, 313 (1991).
Lachenbruch, C. A., "A Network Thermodynamic Model of Kidney Perfusion," PhD Diss., University of Texas at Austin, TX (1995).
Levin, R. L., E. G. Cravalho, and C. G. Huggins, "A Membrane Model Describing the Effect of Temperature on the Water Conductivity of Erythrocyte Membranes at Subzero Temperatures," *Cryobiology*, **13**, 415 (1976).

Levin, R. L., E. G. Cravalho, and C. E. Huggins, "The Effect of Solution Non-Ideality on RBC Volume Regulation," *Biochim. Biophys. Acta*, **465**, 549 (1977).
Love, R. M., "The Freezing of Animal Tissue," *Cryobiology*, H. T. Meryman, ed., Chap. 7, Academic Press, London (1966).
Lovelock, J. E., "Haemolysis of Human Red Blood-Cells by Freezing and Thawing," *Biochim. Biophys. Acta*., **10**, 414 (1953).
Marcove, R. C., J. Sadrieh, A. G. Huvos, and H. Grabstald, "Cryosurgery in the Treatment of Solitary or Multiple Bone Metastases from Renal Cell Carcinoma," *J. Urol*., **108**, 540 (1972).
Mazur, P., "Kinetics of Water Loss from Cells at Subzero Temperatures and the Likelihood of Intracellular Freezing," *J. Gen. Physiol*., **47**, 347 (1963).
Mazur, P., "Cryobiology: The Freezing of Biological Systems," *Science*, **168**, 939 (1970).
McGrath, J. J., "Membrane Transport Properties," *Low Temperature Biotechnology: Emerging Applications and Engineering Contributions*, J. J. McGrath and K. R. Diller, eds., ASME BED, Vol. 10; HTD, Vol. 98, 273 (1988).
Meryman, H. T., "Review of Biological Freezing," *Cryobiology*, H. T. Meryman, ed., Academic Press, New York (1966).
Montgomery, D. C., and G. C. Runger, *Applied Statistics and Probability for Engineers*, Wiley, New York (1994).
Neel, H. B., A. S. Ketcham, and W. G. Hammond, "Cryonecrosis of Normal and Tumor-Bearing Rat Liver Potentiated by Inflow Occlusion," *Cancer*, **28**, 1211 (1971).
Nugent, L. J., and R. K. Jain, "Extravascular Diffusion in Normal and Neoplastic Tissues," *Cancer Res*., **44**, 238 (1984).
Onik, G., B. Rubinsky, G. Watson, and R. J. Ablin, "Percutaneous Prostate Cryoablation," Quality Medical Publishing, St. Louis, MO (1995).
Pazhayannur, P. V., and J. C. Bischof, "Measurement and Simulation of Water Transport during Freezing in Mammalian Liver Tissue," *ASME J. of Biomech. Eng*., **119**, 269 (1997).
Pitt, R. E., "Cryobiological Implications of Different Methods of Calculating the Chemical Potential of Water in Partially Frozen Suspending Media," *Cryo-Letters*, **11**, 227 (1990).
Rabb, J. M., M. L. Renaud, P. A. Brandt, and C. W. Witt, "Effect of Freezing and Thawing on the Microcirculation and Capillary Endothelium of the Hamster Cheek Pouch," *Cryobiology*, **11**(6), 508 (1974).
Rabin, Y., and A. Shitzer, "Numerical Solution of the Multidimensional Freezing Problem during Cryosurgery," *ASME J. of Biomech. Engineering*, **120**, 32 (1998).
Roberts, K. P., D. J. Smith, H. Ozturk, A. Kazem, P. V. Pazhayannur, J. C. Hulbert, and J. C. Bischof, "Biochemical Alterations and Tissue Viability in AT-1 Prostate Tumor Tissue after *in vitro* Cryodestruction," *Cryo-Letters*, **18**, 241 (1997).
Rubinsky, B., and M. Ikeda, "A Cryomicroscope using Directional Solidification for Controlled Freezing of Biological Material," *Cryobiology*, **22**, 55 (1985).
Rubinsky, B., C. Y. Lee, J. Bastacky, and T. L. Hayes, "The Mechanism of Freezing Process in Biological Tissue," *Cryo-Letters*, **8**, 370 (1987).
Rubinsky, B., and D. E. Pegg, "A Mathematical Model for the Freezing Process in Biological Tissue," *Proc. R. Soc. Lond., Series B: Biological Sciences*, **234**, 343 (1988).
Smith, D. J., S. J. Josephson, and J. C. Bischof, "A Model of Cryosurgical Destruction in AT-1 Prostate Tumor Based on Cellular Damage Mechanisms," *Advances in Heat and Mass Transfer in Biotechnology*, S. Clegg, ed., ASME BED, Vol. 37; HTD, **355**, 149 (1997).
Smith, D. J., M. Schulte, and J. C. Bischof, "The Effect of Dimethylsulfoxide on the Water Transport Response of Rat Hepatocytes During Freezing," *ASME J. of Biomech. Eng*., **120**(5), 549 (1998).
Swabb, E. A., J. Wei, and P. M. Gullino, "Diffusion and Convection in Normal and Neoplastic Tissues," *Cancer Res*., **34**, 2814 (1974).
Tatsutani, K., B. Rubinsky, G. Onik, and R. Dahiya, "Effect of Thermal Variables on Frozen Human Primary Prostatic Adenocarcinoma Cells," *Adult Urology*, **48**, 441 (1996).
Toner, M., "Nucleation of Ice Crystals in Biological Cells," *Advances in Low Temperature Biology*, P. L. Steponkus, ed., JAI Press Ltd., London, Vol. 2, p. 1 (1993).
Trump, B. F., P. J. Goldblatt, C. C. Griffin, V. S. Waravdekar, and R. E. Stowell, "Effects of Freezing and Thawing on the Ultrastructure of Mouse Parenchymal Cells," *Laboratory Investigation*, **13**(9), 967 (1964).
Yarmush, M. L., M. Toner, J. C. Y. Dunn, A. Rotem, A. Hubel, and R. G. Tompkins, "Hepatic Tissue Engineering—Development of Critical Technologies," *Annals of the New York Academy of Sciences*, **665**, 238 (1992).

Appendix: Resistance of Interstitial Spaces to Water Transport

A simple analysis is performed to show that the resistance of interstitial spaces to water transport is negligible in comparison to the resistance of the tumor tissue cell membrane. Assuming (a) that the interstitial spaces could be accounted for in the Krogh model as a concentric cylinder with a radius r_{int} around the microvascular channel of radius r_{vas}, and (b) that the interstitial spaces and vascular spaces represent 35% and 7% of the total volume, ($L \cdot \Delta X^2$, where $L = 18.1$ μm and $\Delta X = 17.9$ μm), we can calculate the radius of vascular cylinder as $0.07 \cdot \Delta X^2 = \pi \cdot r_{\text{vas}}^2$ and the radius of the interstitial cylinder as $0.35 \cdot \Delta X^2 = \pi \cdot (r_{\text{int}}^2 - r_{\text{vas}}^2)$. Substituting and solving: r_{int} and r_{vas} are 6.5 and 2.7 μm, respectively, and the interstitial volume is 2029.8 μm^3 (or $0.35 \cdot \Delta X^2 \cdot L$). One can now represent the resistance offered by interstitial spaces to water transport R_{int}, using Darcy's law (in an analogous manner to resistance offered to one-dimensional conductive heat transfer in cylindrical coordinates using Fourier's law)

$$R_{\text{int}} = \frac{(2 \cdot \pi \cdot r_{\text{int}} \cdot L) \cdot \ln\left(\dfrac{r_{\text{int}}}{r_{\text{vas}}}\right)}{2 \cdot \pi \cdot L \cdot \left(\dfrac{k_w \cdot \upsilon_w}{\eta_w}\right)} \tag{A1}$$

where k_w is the interstitial hydraulic conductivity to water (mol/m); υ_w is the molar volume of water (1.8×10^{-5} m^3/mol); and η_w is the viscosity of water (1.792×10^{-3} N·s/m^2). Although the *in vivo* measurement of the interstitial conductivity k_w is extremely difficult, a few investigators have attempted to quantify this value, as noted by Jain (1987), and is approximately in the order of 10^{-13} mol/m (Swabb et al., 1974; Lachenbruch, 1995). Substituting these values in Eq. A1, the value of R_{int} is $\sim 10^9$ N·s/m^3. In the text we measured a membrane permeability of $\sim 10^{-13}$ m^3/N·s or a membrane resistance (inverse of the membrane permeability), R_{mem} of $\sim 10^{13}$ N·s/m^3. Therefore, the resistance of the interstitial spaces to water transport is $\sim 10^{-4}$ times the resistance of membrane to water transport, and, hence, its effect on water transport is negligible.

Manuscript received May 11, 1998, and revision received Dec. 10, 1998.